

Cellular uptake and imaging studies of gadolinium-loaded single-walled carbon nanotubes as MRI contrast agents

Annie M. Tang^{a,b}, Jeyarama S. Ananta^c, Hong Zhao^a, Brandon T. Cisneros^c, Edmund Y. Lam^b, Stephen T. Wong^a, Lon J. Wilson^c and Kelvin K. Wong^{a*}

We quantify here, for the first time, the intracellular uptake (J774A.1 murine macrophage cells) of gadolinium-loaded ultra-short single-walled carbon nanotubes (gadonanotubes or GNTs) in a 3 T MRI scanner using R_2 and R_2^* mapping *in vitro*. GNT-labeled cells exhibited high and linear changes in net transverse relaxations (ΔR_2 and ΔR_2^*) with increasing cell concentration. The measured ΔR_2^* were about three to four times greater than the respective ΔR_2 for each cell concentration. The intracellular uptake of GNTs was validated with inductively coupled plasma optical emission spectrometry (ICP-OES), indicating an average cellular uptake of 0.44 ± 0.09 pg Gd per cell or 1.69×10^9 Gd³⁺ ions per cell. Cell proliferation MTS assays demonstrated that the cells were effectively labeled, without cytotoxicity, for GNTs concentrations $\leq 28 \mu\text{M}$ Gd. *In vivo* relaxometry of a subcutaneously-injected GNT-labeled cell pellet in a mouse was also demonstrated at 3 T. Finally, the pronounced R_2^* effect of GNT-labeled cells enabled successful *in vitro* visualization of labeled cells at 9.4 T. Copyright © 2010 John Wiley & Sons, Ltd.

Keywords: magnetic resonance imaging; cellular imaging; MRI contrast agent; single-walled carbon nanotubes; gadonanotubes

1. INTRODUCTION

Since their laboratory-scale synthesis in 1993, single-walled carbon nanotubes (SWCNTs) have garnered considerable attention in the field of technology and biomedical research (1,2). SWCNTs can be visualized as a single sheet of graphene rolled up seamlessly to form a cylindrical tube. The external all-carbon surface and the hollow interior of SWCNTs provides them with a unique combination of structural properties for internal nanoscale confinement, for external surface functionalization for biological targeting and biocompatibility, and for multi-functional drug delivery (3–8). As such, functionalized SWCNTs have been proposed as carriers for efficient delivery of a wide range of biomolecules such as genes, vaccine and other drugs to targeted sites for therapeutic purposes (5–7,9).

The inherent optical properties of SWCNTs have been utilized to track them by various imaging modalities. For example, *in vitro* imaging of SWCNTs in cells and *ex vivo* imaging in animal tissue have been demonstrated using near-infrared (NIR) fluorescence imaging (10,11), Raman spectroscopy (12) and X-ray fluorescence microscopy (13). In addition, several agents such as iodine (14), fluorescent molecules (15), iron oxide (16) and radiotracers (17,18) have been attached either to SWCNT surfaces or encapsulated within their hollow interiors for imaging. By and large, optical microscopy remains the most popular imaging modality for visualization of SWCNTs in cells and tissue. In general, however, optical imaging suffers from low tissue penetration. In most cases, evaluation of SWCNT delivery by optical imaging can only be confirmed by *in vitro* experiments or by examining *ex vivo* tissue samples, and the

samples often require proper staining for better visualization (19).

In order to track the SWCNT-based drug delivery platforms *in vivo* and follow the post-treatment biodistribution and their ultimate biological fate, real-time visualization and quantification of the SWCNT core itself are desirable. Among various diagnostic imaging modalities, MRI offers the advantages of non-ionizing, non-invasive, multi-planar capabilities that favor the long-term tracking of SWCNTs *in vivo*. Currently, molecular and cellular imaging using MRI mostly revolves around the use of iron oxide based r_2 agents, such as superparamagnetic iron oxide nanoparticles (SPIOs) or micron-sized iron oxide particles (MPIOs) (20–22). Recent studies have shown that gadolinium-loaded ultra-short single-walled carbon nanotubes (gadonanotubes or GNTs) can be used as high-performance r_1 and r_2 MRI contrast

* Correspondence to: K. K. Wong, 6565 Fannin Street, B5-017, Houston, TX 77030, USA.

E-mail: KWong@tmhs.org

a A. M. Tang, H. Zhao, S. T. Wong, K. K. Wong
Bioengineering and Bioinformatics Program, The Methodist Hospital
Research Institute & Weill Cornell Medical College Houston, TX 77030, USA

b A. M. Tang, E. Y. Lam
Department of Electrical and Electronic Engineering, The University of Hong
Kong, Pokfulam Road, Hong Kong

c J. S. Ananta, B. T. Cisneros, L. J. Wilson
Department of Chemistry and Richard E. Smalley Institute for Nanoscale
Science and Technology, Rice University, Houston, TX 77005, USA

agents (23–25). GNTs are prepared by encapsulating Gd^{3+} -ion clusters within the hollow interior of a SWCNT nanocapsule. GNTs outperform traditional gadolinium chelate MRI contrast agents in r_1 relaxivity by about 40 times at clinical field strengths, and they are an efficient R_2 agent (25). In fact, subcutaneous injection of GNTs dispersed in a biocompatible surfactant (pluronic F-127) has recently shown excellent negative contrast *in vivo* (24).

The objective of the present study was to investigate the potential of quantifying intracellular uptake of GNTs in MRI, using R_2 and R_2^* mapping at different GNT-labeled cell concentrations *in vitro*. Quantitative R_2 and R_2^* mappings allow non-invasive measurement of cellular uptake of GNTs, with the potential to monitor the *in vivo* performance of SWCNT-assisted drug delivery by MRI (26). In the course of our investigation, *in vitro* cytotoxicity studies were carried out to optimize the GNTs concentration for cell labeling and *in vivo* visualization and quantification of a subcutaneously injected GNT-labeled cell pellet in a mouse was also performed using a 3 T clinical system. Finally, *in vitro* cell visualization using GNT-labeled cells has also been demonstrated at 9.4 T.

2. RESULTS

2.1. GNT solution characterization

The relaxations of the biocompatible GNTs solution were characterized prior to cell labeling. Table 1 shows the relaxation rates of the GNTs solution at 3 T. The coefficients of determination of the two-parameter non-linear fittings, which represent the quality of the fittings, are also shown. The GNTs solution had an R_1 relaxation rate of 7.50 s^{-1} , equivalent to the r_1 relaxivity of $67.57\text{ mM}^{-1}\text{ s}^{-1}$ (per Gd^{3+} ions). R_2 and R_2^* relaxation rates were 47.04 and 49.88 s^{-1} , respectively, with the R_2^* value about 6% higher than R_2 . All the fitted curves had the R_2 values closed to 1, indicating the relaxation curves excellently fit the measured data.

2.2. GNT labeling

Figure 1 shows the microscopic images of the GNT-labeled J774A.1 cells. The labeled cells appeared black in the intracellular space under bright-field microscopy, having the same color as the free GNTs (Figure 1a). Compared with the Hoechst blue nucleus fluorescent image that was captured at identical location, it was clearly seen that the gadonanotubes accumulated mostly in the cytoplasm, without getting into the nucleus (Figure 1b). Figure 2 shows the cell viability test using MTS assay at four different concentrations of GNTs. The result indicated that there was no significant cytotoxicity at GNTs concentration below $27.75\text{ }\mu\text{M Gd}$, and therefore, this concentration was used for all the subsequent cell-labeling experiments. The ICP results indicated an average

Table 1. Relaxation rates of the GNTs solution suspension measured at 3T, in a 1 cm^3 syringe parallel to the main B_0 field. The coefficient of determination (R^2) of each estimation is also shown

Concentration ($\mu\text{M Gd}$)	Relaxation rate (s^{-1})		
	R_1 (R^2)	R_2 (R^2)	R_2^* (R^2)
111	7.50 (0.98)	47.04 (0.99)	49.88 (0.99)

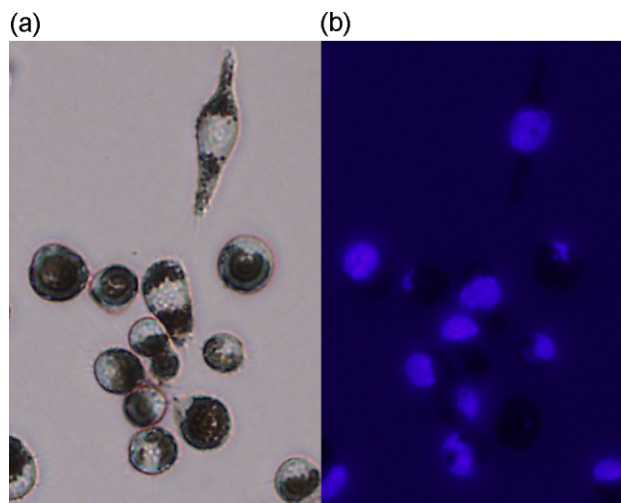


Figure 1. Microscopic images of GNTs-labeled J774A.1 cells. (a) Bright field image of cells labeled with GNTs incubated at a concentration of $27\text{ }\mu\text{M Gd}$, showing the bio-distribution of the GNTs in the intracellular space. (b) Blue fluorescence image of the labeled cells captured at identical position with the Hoechst 33342 nucleus stain.

cellular uptake of $0.44 \pm 0.09\text{ pg Gd}$ per cell, corresponding to an uptake of $19.3 \pm 3.8\text{ pg GNTs}$ per cell.

2.3. In vitro MRI imaging

Figure 3 shows the ΔR_2 and ΔR_2^* relaxation measurements of *in vitro* phantoms at 3 T for an increasing number of GNT-labeled cells homogeneously distributed in 1.0% agarose gel. ΔR_2 and ΔR_2^* represent the net relaxations of the labeled cells, with contribution from the agarose gel as well as the background field inhomogeneities subtracted. The ΔR_2 and ΔR_2^* effects increase linearly (with $R^2 = 0.98$ and 0.93 respectively) with increasing number of labeled cells. This correlates well to the ICP results in Table 2, showing increasing concentration of cell-bounded GNTs in the phantoms. The measured ΔR_2^* value for each cell phantom was about three to four times greater than the corresponding ΔR_2 value, and with the slope of the overall ΔR_2^* effect being more than twice that of the ΔR_2 effect (3.57 versus 1.58). The mean and standard deviation of the plotted values were computed by acquiring ROIs at multiple slices at each phantom.

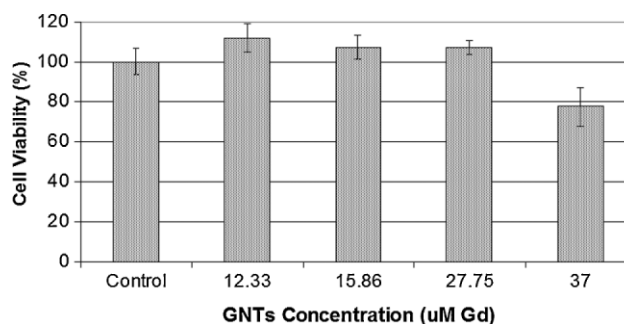


Figure 2. Cell proliferation test with MTS assay. The *in vitro* cytotoxicity of GNTs was tested at four different concentrations. Each concentration was performed in triplicate and the mean \pm standard deviation of each concentration was shown. GNTs-labeled cells had insignificant differences in cell viability at gadonanotubes concentration below $27.75\text{ }\mu\text{M Gd}$, while the cell viability dropped to 78% at concentration of $37\text{ }\mu\text{M Gd}$.

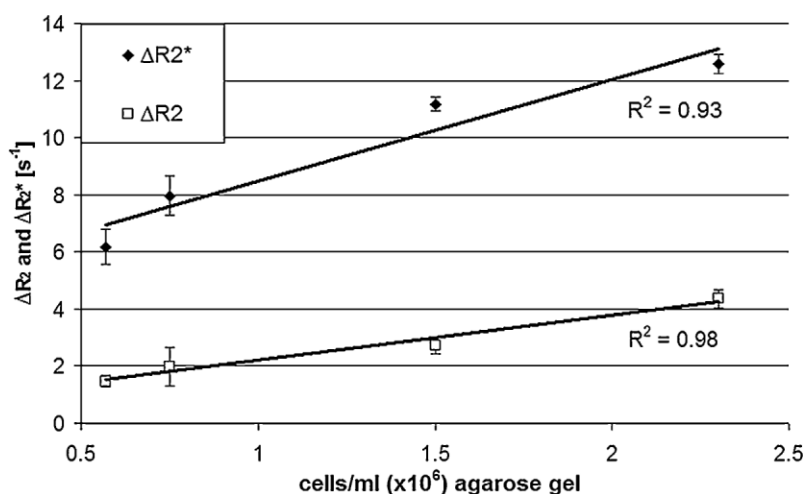


Figure 3. ΔR_2 and ΔR_2^* relaxation measurements of the GNTs-labeled cell phantoms with increasing number of labeled cells in 1.0% agarose gel at 3 T. The net relaxation, ΔR_2 and ΔR_2^* were calculated by subtracting the measured R_2 and R_2^* values of the GNTs-labeled cell phantoms with that of the unlabeled cell phantom controls. Error bars represent one standard deviation.

The standard deviations were small ($<10\%$) in most of the measurements, suggesting that the labeled cells were homogeneously distributed within the phantoms. R_1 relaxations were also measured in all phantoms. There was no significant increase in R_1 relaxation as compared to the control phantoms. All showed a T_1 value of about 1600 ± 60 ms, corresponding to a R_1 value of $0.625 s^{-1}$.

Figure 4 shows the T_2^* -weighted image of the sparsely-distributed *in vitro* cell phantom ($5500 \text{ cells ml}^{-1}$) at 9.4 T, demonstrating labeled-cells visualization at high-field MRI. The imaging spatial resolution was $50 \times 50 \times 50 \mu\text{m}$. Two types of reconstruction methods are shown for comparison. Figure 4(b) shows the reconstruction using the susceptibility weighted imaging (SWI) method (27), while Figure 4(a) shows the simple magnitude image. Dark spots were clearly seen in both of the images, but with the spots appearing much clearer in SWI reconstructed image.

2.4. In vivo MRI imaging

The *in vivo* relaxometry measurements of the subcutaneously injected GNT-labeled cell pellets in mice at 3 T demonstrated the feasibility of monitoring and quantifying the labeled cells *in vivo* in clinical-grade MRI systems. Figure 5 shows the T_2^* map, and the R_2^* map of the labeled- and unlabeled-cell pellets overlaid onto an anatomical image. As shown in Figure 5(a), the T_2^* mapping of the labeled-cell pellet on the left of the dorsal flank was

substantially dimmer (yellow arrow) than the surrounding tissue, whereas the unlabeled-cell control at the right side showed no significant difference from the surrounding tissue. The mean T_2^* value of the labeled-cell pellet was 16.83 ± 5.30 ms, corresponding to a mean R_2^* value of $65.50 \pm 21.80 s^{-1}$. For the unlabeled-cell control, the mean T_2^* value was 40.58 ± 16.26 ms, corresponding to a mean R_2^* value of $28.60 \pm 11.6 s^{-1}$. Thus, the mean R_2^* of the labeled-cell pellet was significantly higher (ca 2.3 times) than that of the unlabeled-cell pellet control. The mean R_2 values for both gel pellets were above 0.8 (0.87 and 0.86, respectively), indicating a reliable estimation of the fitted results from the measured data.

3. DISCUSSIONS

In this study, we have quantified, for the first time, the intracellular uptake of GNTs based on transverse relaxations (ΔR_2 and ΔR_2^*) at 3 T *in vitro*, with increasing concentration of labeled cells dispersed in homogenous agarose gel phantoms. The GNT-labeled cells exhibited greater (a few times greater than ΔR_2) and linear ΔR_2^* with the concentration of Gd^{3+} ions in $\mu\text{g ml}^{-1}$ range for all phantoms. Therefore, ΔR_2^* can be regarded as a sensitive and quantifiable method for visualizing GNTs upon cell internalization at 3 T. The established linear correlation between the ΔR_2^* values and the labeled-cell concentration or Gd^{3+} ions allowed quantitative monitoring of cell population *in vivo*. As shown in the *in vivo* feasibility study, the mean ΔR_2^* of the labeled-cell pellet was about $36.90 s^{-1}$ with a cell concentration of $8 \times 10^6 \text{ cells ml}^{-1}$. This corresponds well with the expected value from the *in vitro* ΔR_2^* mapping (by extrapolating the linear regression line to the corresponding cell concentration).

For the measured R_1 , ΔR_2 and ΔR_2^* effects of the cell phantoms, it was clearly seen that ΔR_2^* were a few times greater than ΔR_2 at all concentrations, and the cell phantoms exhibited no R_1 signal enhancements at all at 3 T. The cell phantom results were different from that of GNT solution (when not internalized in cells). The GNTs solution showed a large R_1 effect and the R_2^* value was only slightly greater ($\sim 6\%$) than that of R_2 .

The lack of R_1 enhancement and increase in R_2 and R_2^* upon intracellular uptake in macrophage cells could be attributed to the compartmentalization of GNTs inside the cells. The high

Table 2. The total amount of Gd^{3+} ions in phantoms determined by inductively coupled plasma optical emission spectrometry (ICP-OES). The corresponding ΔR_2 and ΔR_2^* values are plotted in Fig. 3

Cells ml^{-1}	$[\text{Gd}^{3+}] \mu\text{g ml}^{-1}$
2.3×10^6	0.85
1.5×10^6	0.61
0.75×10^6	0.43
0.57×10^6	0.25

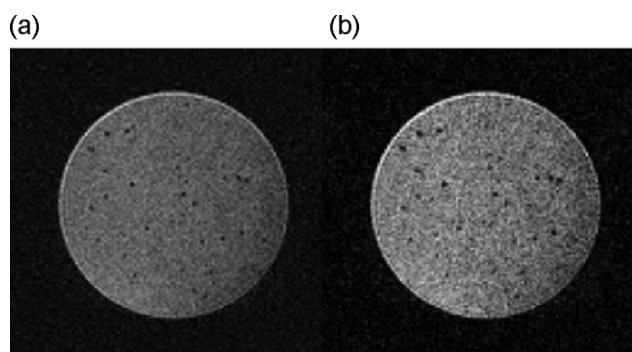


Figure 4. T_2^* -weighted image of sparsely distributed GNTs-labeled J774A.1 cells ($5500 \text{ cells ml}^{-1}$) suspended in 1.0% agarose gel at 9.4 T, using 3D SPGR sequence. (a) Magnitude image and (b) SWI image. SWI image was obtained by multiplying the phase mask with the original magnitude image. Dark spots were clearly seen in both images, but with the susceptibility-induced effects appearing more obvious in the SWI image.

density packing of GNTs inside the cells induced susceptibility effects resulting in substantial increase in R_2 and R_2^* relaxations. These results agree with previous studies which investigated the

change in transverse relaxations upon cell internalization of iron oxide particles (26,28–30). Although a superparamagnetic Gd-based agent (GNT) was used in our study, the transverse relaxation mechanisms upon cell internalization is believed to be similar to iron oxide, since the transverse relaxation is simply induced by through-space susceptibility effects due to the presence of metal content. In addition to the Gd^{3+} ions, the GNTs also contain other metal impurities from the synthesis of the precursor SWCNT materials. The metal catalyst impurities have been shown to impart R_2 characteristics on SWCNTs (precursor to GNTs) (31). For the R_1 relaxation, the quenching of the relaxation upon cellular uptake is probably due to the slow transport of water across the cell membrane. Further investigation may be needed to explore the cellular uptake mechanism and the distributions of GNTs in cells, as well as the correlations between the intracellular localization of GNTs and the water relaxation mechanisms.

Note that, in our 3T study, a relatively limited range of TE s (10–125 ms depending on materials) was applied for R_2 and R_2^* estimations. There is a possibility that the labeled cells may have ultra-short T_2 components in which our current range of TE s (10 ms or more) ceases to detect. This is a limitation of our experiments, as the clinical MRI's pulse sequences restricted the

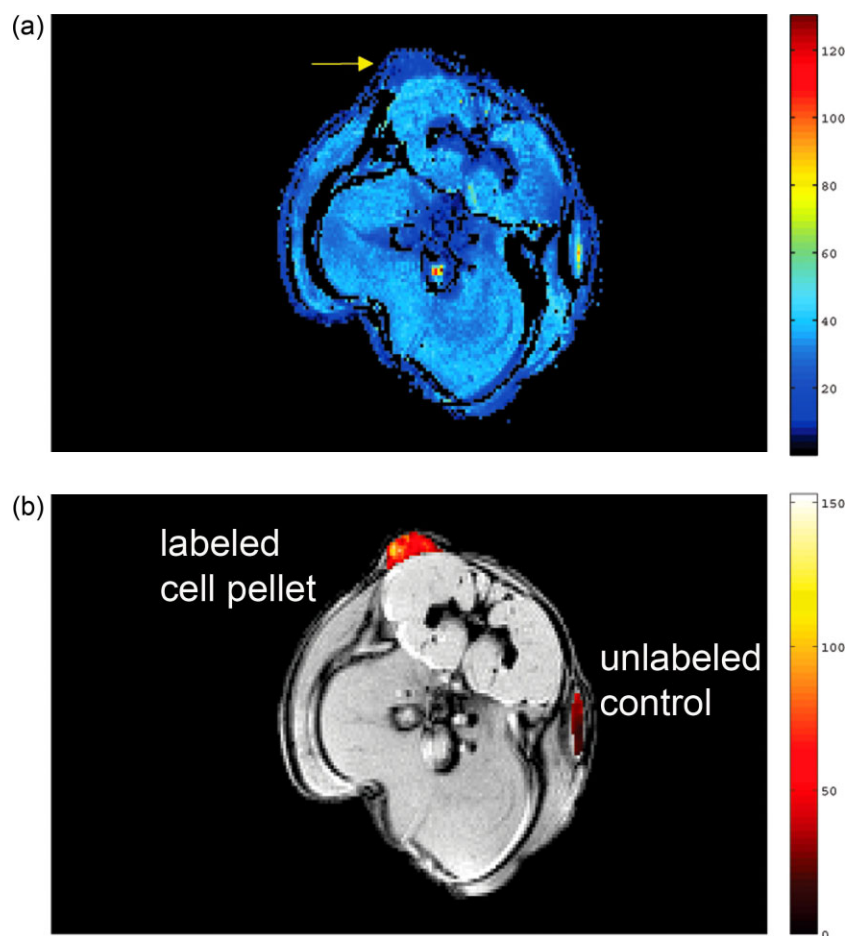


Figure 5. *In vivo* relaxometry measurements of subcutaneously injected cell pellets in a mouse at 3 T. Agarose gel pellets containing GNTs-labeled cells and unlabeled cells (4×10^5 cells per pellet) with volume of about $50 \mu\text{L}$ were injected into the left and right dorsal flank of a C57BL/6 mouse respectively. (a) T_2^* map (in ms) of the injected cell pellets, and (b) R_2^* mapping (in s^{-1}) with two ROIs drawn at the cell pellets and overlaid onto an anatomical T_2 -weighted image.

shortest TE parameter being applied. Further studies could be done to explore the T_2 effects of labeled-cells at various range of TE s, using ultra-short T_2^* or ultra-short TE (UTE) techniques (32).

The strong R_2^* effect of GNTs upon cell internalization has allowed labeled cells to be visualized *in vitro*. Cell visualizations in MRI have been demonstrated using MPIOs and SPIOs (20,33). To visualize labeled cells using MRI, heavy labeling with iron oxide-based contrast agent is required. Herein, we were able to visualize labeled cells as dark spots in MRI using GNTs at 9.4 T. The high-performance gradient at 9.4 T helps to achieve an image resolution of 50 μm isotropic, which is not possible with the gradient performance on clinical systems. The observed signal voids originated from the presence of superparamagnetic GNTs in the cells, which induced a magnetic susceptibility effect in their local regions, generating field inhomogeneity and thus extra de-phasing around the those regions. The SWI reconstruction utilized the phase image to generate a phase mask and multiplied it by the original magnitude image, which further enhanced the contrast between regions with different susceptibilities. SWI is a pure post-processing technique that requires no extra imaging time.

The ICP-OES result showed that the intracellular uptake of GNTs in macrophages was 0.44 ± 0.09 pg Gd per cell on average, corresponding to 1.69×10^9 Gd^{3+} ions per cell. This result was consistent with a previous study using serine-derivatized GNTs to label a MCF-7 human breast cancer cell line (34), and was two orders of magnitude greater (10^9 vs 10^7 Gd^{3+} ions per cell) than when water-soluble gadofullerenes were used to label mesenchymal stem cells (35). In the present studies, we have used a macrophage cell line for demonstration. It has been reported that macrophages can be labeled with SPIOs reproducibly at high loading levels via phagocytosis (33). Our result have shown that macrophages could also be reliably labeled with GNTs at high loading levels (~ 20 pg per cell), without a transfection agent or advanced labeling techniques. This property greatly facilitated GNTs being used for robust intracellular uptake quantifications and for cell visualization. Note that the quantifications may have to be repeated when different cell lines are used, as different cell lines may have different cellular uptake capabilities.

GNTs are a new class of SWCNTs-derived MRI contrast agent, and some concerns have been raised about the toxicity effects of SWCNTs-based materials (36–38). Our cytotoxicity studies here have revealed that GNT-labeled cells exhibited 100% viability as compared with unlabeled control, when the GNT concentration was $ca \leq 28$ μM Gd. Further increasing the concentration would lead to a decrease in cell viability to about 80% at 37 μM Gd. This result suggested that 28 μM Gd is about the best concentration to use for GNTs cell-labeling experiment. Finally, we observed that the GNT-labeled cells were still growing inside the gel phantoms, several days after the MRI imaging was completed.

4. CONCLUSION

The exceptionally large and linear transverse relaxations of GNTs provide the material with sufficient sensitivity for cellular imaging in clinical 3 T MRI systems, and permit cell visualization at 9.4 T using better spatial resolution. Future studies with GNTs include the determination of their minimum detection threshold for cellular imaging, the intracellular uptake mechanism of the materials and the relaxations dependency on sub-cellular localization.

5. EXPERIMENTAL

5.1. Gadonanotube synthesis

Full-length, SWCNTs produced by electric-arc discharge were cut into ultra-short carbon nanotubes (US tubes) of length 20–80 nm and diameter 1 nm by fluorination followed by pyrolysis at 1000 °C under an inert atmosphere (39). The cutting process reduced the amount of metal catalyst impurities ($<3\%$) while creating defect sites in the US tube sidewalls. The defect sites allow the loading of ions and molecules into the interior of the US tubes (23). Owing to their hydrophobic nature, the US tubes exist in the form of bundles. To obtain a homogenous sample, US tubes were reduced using Na^0/THF to produce predominantly individual tubes or small bundles (3). The reduced US tubes were immersed in aqueous GdCl_3 solution (1 mg ml^{-1}) and vigorously sonicated for 60 min. The solution was left unperturbed overnight to allow the resulting GNTs to flocculate for easy filtration. The GNTs were then washed with de-ionized water several times to remove external Gd^{3+} ions adhered to the US tube sidewalls and air dried.

To prepare a stable and biocompatible GNTs solution (suspension) for MRI measurements and cell-labeling studies, 10 mg of GNTs was dispersed in 10 mL of 1.0% (w/v) Pluronic® F108 solution using a probe sonicator. The resulting suspension was centrifuged at 3200 rpm for 15 min to remove any large aggregates. The supernatant was collected and dialyzed (50 000 MW cut-off membrane) against running water for 3 days to remove excess surfactant. The Gd^{3+} -ion concentration of the stable GNTs suspension was determined using inductively coupled plasma optical emission spectrometry (ICP-OES, Perkin-Elmer Optima 3200V), giving a final concentration of 111 μM Gd. About 1 mL of the GNTs suspension was transferred to a 1 cm^3 syringe for MRI measurements.

5.2. Cell culture and gadonanotubes labeling

J774A.1 mouse macrophages cell line (ATCC, Manassas, VA, USA) was cultured at 37 °C and 5% CO_2 in 100 \times 20 mm tissue culture dishes using standard cell culture media, containing Dulbecco's modified Eagle medium (DMEM, Invitrogen) with 10% fetal bovine serum (FBS, Invitrogen) and 1% penicillin–streptomycin (S/P, Fisher Scientific). *In vitro* cytotoxicity of the GNTs was first tested in a 96-well micro-plate using a MTS-based cell proliferation assay (CellTiter 96® Aqueous One Solution Assay, Promega). To determine the highest concentration of GNTs solution suspension that could be used for cell labeling without significant cytotoxicity, four different concentrations of GNTs (37.0, 27.75, 15.86, and 12.33 μM Gd) were tested, using unlabeled cells as control. Each concentration was tested in triplicate.

For GNTs labeling, 5×10^5 cells per well were plated in six-well plates for 24 h to allow cell adhesion. The cells were then incubated with the GNTs solution diluted with the standard culture media (final $[\text{Gd}] = 27.75$ μM) as determined in the cell proliferation test, for another 24 h. The labeled cells were then washed twice with phosphate buffered saline (PBS, Invitrogen) to remove any excess CNTs that might be adsorbed on the cell membrane.

5.3. Fluorescence staining and microscopy

To visualize the intra-cellular distribution of the GNTs, Hoechst 33342 dye (Invitrogen Corporation, CA, USA) were used to stain

the nucleus of the labeled cells. Hoechst dye is a cell permeable nucleic acid stain that increases fluorescent intensity when bound to DNA and is commonly used to locate the nucleus in cells. The labeled cells in suspension were incubated with 1 μM Hoechst 33342 at room temperature for 10 min and then examined with fluorescence microscopy (Olympus IX51). The excitation and emission spectra for Hoechst dye are 350 and 460 nm, respectively. Bright field microscopic images were also captured at identical positions, to observe the distribution of gadonanotubes in the cells as well as identifying the locations of the nucleus.

5.4. In vitro MRI phantom preparation

For *in vitro* MRI experiments, a portion of the labeled cells was re-suspended in an equal volume of $2 \times$ DMEM culture media and 2% agarose gel (Type VII, Sigma) at 37 °C, and transferred to 1 cm^3 syringes for making MRI phantoms. The process was performed carefully to avoid air bubbles inside the 1 cm^3 syringes and premature gelling of the agarose mixture. Four different concentrations of homogeneity-dispersed labeled cells phantoms (2.3×10^6 , 1.5×10^6 , 0.75×10^6 and 0.57×10^6 cells ml^{-1}) were prepared for relaxation measurements at 3 T. Another four phantoms at the same concentration of unlabeled cells were also prepared as controls. In addition, a sparsely distributed labeled cell phantom (5500 cells ml^{-1}) was also prepared for cell visualization at 9.4 T high-field MRI. All the phantoms were cylindrical in shape and were about 3.5 cm long.

The total amount of Gd^{3+} ions in each of the phantom was determined by ICP-OES. From the concentration of Gd^{3+} ions and the total number of cells, the average uptake of Gd^{3+} ion by each cell was calculated. The measurements were performed in triplicate and the mean and standard deviations of the results were calculated.

5.5. Animal Preparation

For *in vivo* relaxometry, a portion of the GNT-labeled cells were suspended in PBS and mixed with 1% agarose gel at 37 °C for subcutaneous injection into the dorsal flank of a female C57BL/6 mouse (Charles River, Wilmington, MA, USA). A total of 4×10^5 labeled cells per pellet with a volume of 50 μl was injected into the left dorsal flank of the mouse. The injection was done carefully to create an inflated bulb for easy localization in MRI. Another equivalent amount of unlabeled cell pellet (4×10^5 cells) in 1% agarose gel was also injected into right side as control. The animal was then immediately transferred to the 3 T MRI unit for imaging. The animal experiment was approved by the Institutional Animal Care and Use Committee of The Methodist Hospital Research Institute.

5.6. MRI

MRI was performed in a whole-body 3 T system (General Electric, Milwaukee, WI) using a 35 mm inner diameter custom-built quadrature coil for *in vitro* and *in vivo* relaxation measurements, and in a 9.4 T system (Bruker Biospec 94/20 USR) for the labeled-cells visualization.

For *in vitro* relaxations studies at 3 T, the 1 cm^3 syringes were positioned at the iso-center of the magnetic bore, with the cylindrical axis parallel to the main B_0 field. R_1 relaxation of the GNTs solution suspension was measured using a 2D spin-echo inversion recovery (IR) sequence with the following imaging

parameters: $TR/TE = 5000/15$ ms, $IR = 60\text{--}150$ ms with 10 ms increment and $200\text{--}800$ ms with 100 ms increment, $FOV = 5.0$ cm, $\text{matrix} = 128 \times 128$, $NEX = 1$, $\text{thickness} = 1$ mm, $\text{no. of slices} = 4$. R_2 and R_2^* relaxations of the solution were also measured using 2D spin-echo and gradient echo sequences respectively, with $TR = 1500$ ms, $TE = 10\text{--}45$ ms with 5 ms of increment, $FOV = 5.0$ cm, $\text{matrix} = 192 \times 192$, $NEX = 1$. Circular ROIs were drawn and the R_1 , R_2 and R_2^* relaxations of the phantoms were computed using non-linear curve fittings of the mean intensity of each ROI in the images using Matlab (Mathworks™, Natick, MA, USA). For the GNT-labeled and unlabeled cells phantoms, the R_1 , R_2 and R_2^* relaxations were measured and computed with similar imaging parameters but using a different range of IRs (50–2500 ms) for R_1 and TE s (15–125 ms with 15 ms increment) for R_2 and R_2^* . The net relaxations, ΔR_2 and ΔR_2^* , of the labeled cell phantoms were calculated by subtracting the R_2 and R_2^* values of the unlabeled-cell phantom controls from the measured R_2 and R_2^* values of the labeled-cell phantoms.

For *in vivo* relaxometry measurement at 3 T, images were acquired by cutting a high-resolution oblique slice covering the injected cell pellets at both sides of the mouse, with the following imaging parameters: $TR = 1500$ ms, $TE = 10\text{--}45$ ms with 5 ms of increment, $FOV = 6.0$ cm, $\text{matrix} = 256 \times 256$, $NEX = 1$. The images obtained were then realigned using SPM2 to reduce motions and fitted mono-exponentially for R_2^* mapping in Matlab. ROIs were drawn at the two pellets at the R_2^* maps and overlaid onto an anatomical image.

For labeled-cell visualization at high-field MRI, the sparsely-distributed labeled-cell phantom (5500 cells ml^{-1}) was imaged at 9.4 T using a 3D spoiled gradient echo sequence ($TR/TE = 3000/40$ ms, $\alpha = 28.6^\circ$, $FOV = 0.64 \times 2.56$ cm, $\text{resolution} = 50 \mu\text{m}$ isotropic, $NEX = 12$). The cylindrical axis of the phantom was placed parallel to the main B_0 field. Reconstruction was done using SWI method, by multiplying the phase mask to the original magnitude image to enhance the contrast effect for better visualization (27).

Acknowledgements

This work was supported in part by the URC of the University of Hong Kong (grant no. 10208648), the Robert A. Welch Foundation (grant no. C-0627) and the Nanoscale Science and Engineering Initiative of the National Science Foundation (grant no. EEC-067452) at Rice University and the Methodist Hospital Research Institute. K. Wong would like to acknowledge the imaging support from Texas Children's Hospital small animal imaging facility.

REFERENCES

1. Bethune DS, Klang CH, de Vries MS, Gorman G, Savoy R, Vazquez J, Beyers R. Cobalt-catalysed growth of carbon nanotubes with single-atomic-layer walls. *Nature* 1993; 363(6430): 605–607.
2. Iijima S. Helical microtubules of graphitic carbon. *Nature* 1991; 354(6348): 56–58.
3. Ashcroft JM, Hartman KB, Mackeyev Y, Hofmann C, Pheasant S, Alemany LB, Wilson LJ. Functionalization of individual ultra-short single-walled carbon nanotubes. *Nanotechnology* 2006; (20): 5033.
4. Chen J, Chen S, Zhao X, Kuznetsova LV, Wong SS, Ojima I. Functionalized single-walled carbon nanotubes as rationally

- designed vehicles for tumor-targeted drug delivery. *J Am Chem Soc* 2008; 130(49): 16778–16785.
5. Shi Kam NW, Jessop TC, Wender PA, Dai H. Nanotube molecular transporters: internalization of carbon nanotube–protein conjugates into mammalian cells. *J Am Chem Soc* 2004; 126(22): 6850–6851.
 6. Bianco A, Kostarelos K, Prato M. Applications of carbon nanotubes in drug delivery. *Curr Opin Chem Biol* 2005; 9(6): 674–679.
 7. Liu Z, Chen K, Davis C, Sherlock S, Cao Q, Chen X, Dai H. Drug delivery with carbon nanotubes for in vivo cancer treatment. *Cancer Res* 2008; 68(16): 6652–6660.
 8. McDevitt MR, Chattopadhyay D, Kappel BJ, Jaggi JS, Schiffman SR, Antczak C, Njardarson JT, Brentjens R, Scheinberg DA. Tumor targeting with antibody-functionalized, radiolabeled carbon nanotubes. *J Nucl Med* 2007; 48(7): 1180–1189.
 9. Liu Z, Winters M, Holodniy M, Dai H. siRNA delivery into human T cells and primary cells with carbon-nanotube transporters. *Angew Chem Int Ed Engl* 2007; 46(12): 2023–2027.
 10. Cherukuri P, Gannon CJ, Leeuw TK, Schmidt HK, Smalley RE, Curley SA, Weisman RB. Mammalian pharmacokinetics of carbon nanotubes using intrinsic near-infrared fluorescence. *Proc Natl Acad Sci USA* 2006; 103(50): 18882–18886.
 11. Welsher K, Liu Z, Darancioglu D, Dai H. Selective probing and imaging of cells with single walled carbon nanotubes as near-infrared fluorescent molecules. *Nano Lett* 2008; 8(2): 586–590.
 12. Liu Z, Davis C, Cai W, He L, Chen X, Dai H. Circulation and long-term fate of functionalized, biocompatible single-walled carbon nanotubes in mice probed by Raman spectroscopy. *Proc Natl Acad Sci USA* 2008; 105(5): 1410–1415.
 13. Bussy C, Cambedouzou J, Lanone S, Leccia E, Heresanu V, Pinault M, Mayne-L'hermite M, Brun N, Mory C, Cotte M, Doucet J, Boczkowski J, Launois P. Carbon nanotubes in macrophages: imaging and chemical analysis by X-ray fluorescence microscopy. *Nano Lett* 2008; 8(9): 2659–2663.
 14. Ashcroft JM, Hartman KB, Kissell KR, Mackeyev Y, Pheasant S, Young S, Van der Heide PAW, Mikos AG, Wilson LJ. Single-molecule I₂@US-tube nanocapsules: a new x-ray contrast-agent design. *Adv Mater* 2007; 19(4): 573–576.
 15. Kim BM, Qian S, Bau HH. Filling carbon nanotubes with particles. *Nano Lett* 2005; 5(5): 873–878.
 16. Choi JH, Nguyen FT, Barone PW, Heller DA, Moll AE, Patel D, Boppart SA, Strano MS. Multimodal biomedical imaging with asymmetric single-walled carbon nanotube/iron oxide nanoparticle complexes. *Nano Lett* 2007; 7(4): 861–867.
 17. Singh R, Pantarotto D, Lacerda L, Pastorin G, Klumpp C, Prato M, Bianco A, Kostarelos K. Tissue biodistribution and blood clearance rates of intravenously administered carbon nanotube radiotracers. *Proc Natl Acad Sci USA* 2006; 103(9): 3357–3362.
 18. McDevitt MR, Chattopadhyay D, Jaggi JS, Finn RD, Zanzonico PB, Villa C, Rey D, Mendenhall J, Batt CA, Njardarson JT, Scheinberg DA. PET imaging of soluble yttrium-86-labeled carbon nanotubes in mice. *PLoS One* 2007; 2(9): e907.
 19. Porter AE, Gass M, Muller K, Skepper JN, Midgley PA, Welland M. Direct imaging of single-walled carbon nanotubes in cells. *Nat Nanotechnol* 2007; 2(11): 713–717.
 20. Shapiro EM, Skrtic S, Sharer K, Hill JM, Dunbar CE, Koretsky AP. MRI detection of single particles for cellular imaging. *Proc Natl Acad Sci USA* 2004; 101(30): 10901–10906.
 21. Bulte JW, Kraitchman DL. Iron oxide MR contrast agents for molecular and cellular imaging. *NMR Biomed* 2004; 17(7): 484–499.
 22. Heyn C, Ronald JA, Ramadan SS, Snir JA, Barry AM, MacKenzie LT, Mikulis DJ, Palmieri D, Bronder JL, Steeg PS, Yoneda T, MacDonald IC, Chambers AF, Rutt BK, Foster PJ. In vivo MRI of cancer cell fate at the single-cell level in a mouse model of breast cancer metastasis to the brain. *Magn Reson Med* 2006; 56(5): 1001–1010.
 23. Sitharaman B, Kissell KR, Hartman KB, Tran LA, Baikov A, Ruskova I, Sun Y, Khant HA, Ludtke SJ, Chiu W, Laus S, Toth E, Helm L, Merbach AE, Wilson LJ. Superparamagnetic gadonanotubes are high-performance MRI contrast agents. *Chem Commun (Camb)* 2005; (31): 3915–3917.
 24. Sitharaman B, Van Der Zande M, Ananta JS, Shi X, Veltien A, Walboomers XF, Wilson LJ, Mikos AG, Heerschap A, Jansen JA. Magnetic resonance imaging studies on gadonanotube-reinforced biodegradable polymer nanocomposites. *J Biomed Mater Res Part A* 2010; 93(4): 1454–1462.
 25. Wong K, Ananta JS, Lin S, Wilson LJ. In vitro relaxivities studies of gadolinium carbon nanotubes at 3T. In *Proceedings 16th Scientific Meeting, International Society for Magnetic Resonance in Medicine*. Toronto, Canada, 2008; p. 1665.
 26. Kuhlper R, Dahnke H, Matuszewski L, Persigehl T, von Wallbrunn A, Allkemper T, Heindel WL, Schaeffter T, Bremer C. R₂ and R₂* mapping for sensing cell-bound superparamagnetic nanoparticles: in vitro and murine in vivo testing. *Radiology* 2007; 245(2): 449–457.
 27. Haacke EM, Xu Y, Cheng YC, Reichenbach JR. Susceptibility weighted imaging (SWI). *Magn Reson Med* 2004; 52(3): 612–618.
 28. Simon GH, Bauer J, Saborovski O, Fu Y, Corot C, Wendland MF, Daldrop-Link HE. T₁ and T₂ relaxivity of intracellular and extracellular USPIO at 1.5 T and 3 T clinical MR scanning. *Eur Radiol* 2006; 16(3): 738–745.
 29. Billotey C, Wilhelm C, Devaud M, Bacri JC, Bittoun J, Gazeau F. Cell internalization of anionic maghemite nanoparticles: quantitative effect on magnetic resonance imaging. *Magn Reson Med* 2003; 49(4): 646–654.
 30. Tanimoto A, Oshio K, Suematsu M, Pouliquen D, Stark DD. Relaxation effects of clustered particles. *J Magn Reson Imag* 2001; 14(1): 72–77.
 31. Ananta JS, Matson ML, Tang AM, Mandal T, Lin S, Wong K, Wong ST, Wilson LJ. Single-walled carbon nanotube materials as T₂-weighted MRI contrast agents. *J Phys Chem C* 2009; 113(45): 19369–19372.
 32. Liu W, Dahnke H, Rahmer J, Jordan EK, Frank JA. Ultrashort T₂* relaxometry for quantitation of highly concentrated superparamagnetic iron oxide (SPIO) nanoparticle labeled cells. *Magn Reson Med* 2009; 61(4): 761–766.
 33. Heyn C, Ronald JA, Mackenzie LT, MacDonald IC, Chambers AF, Rutt BK, Foster PJ. In vivo magnetic resonance imaging of single cells in mouse brain with optical validation. *Magn Reson Med* 2006; 55(1): 23–29.
 34. Hassan AA, Chan BT, Tran LA, Hartman KB, Ananta JS, Mackeyev Y, Hu L, Pautler RG, Wilson LJ, Lee AV. Serine-derivatized gadonanotubes as magnetic nanoprobe for intracellular labeling. *Contrast Media Mol Imag* 2010; 5(1): 34–38.
 35. Anderson SA, Lee KK, Frank JA. Gadolinium-fullerenol as a paramagnetic contrast agent for cellular imaging. *Invest Radiol* 2006; 41(3): 332–338.
 36. Lam CW, James JT, McCluskey R, Hunter RL. Pulmonary toxicity of single-wall carbon nanotubes in mice 7 and 90 days after intratracheal instillation. *Toxicol Sci* 2004; 77(1): 126–134.
 37. Magrez A, Kasas S, Salicio V, Pasquier N, Seo JW, Celio M, Catsicas S, Schwaller B, Forro L. Cellular toxicity of carbon-based nanomaterials. *Nano Lett* 2006; 6(6): 1121–1125.
 38. Worle-Knirsch JM, Pulskamp K, Krug HF. Oops they did it again! Carbon nanotubes hoax scientists in viability assays. *Nano Lett* 2006; 6(6): 1261–1268.
 39. Gu Z, Peng H, Hauge RH, Smalley RE, Margrave JL. Cutting single-wall carbon nanotubes through fluorination. *Nano Letters* 2002; 2(9): 1009–1013.